Materials and Design 87 (2015) 231–237

Contents lists available at ScienceDirect

Materials and Design

journal homepage: www.elsevier.com/locate/jmad

Underlying mechanism of periodical adiabatic shear bands generated in Ti–6Al–4V target by projectile impact

Jintao Liu, Qunbo Fan *, Hongnian Cai, Fuchi Wang

School of Materials Science and Engineering, Beijing Institute of Technology, Beijing 100081, China
National Key Laboratory of Science and Technology on Materials under Shock and Impact, Beijing Institute of Technology, Beijing 100081, China

ARTICLE INFO

Article history:
Received 3 April 2015
Received in revised form 6 August 2015
Accepted 7 August 2015
Available online 12 August 2015

Keywords:
Titanium alloys
Periodical adiabatic shear bands
Finite element analysis
Ballistic test
Fracture

ABSTRACT

Periodical adiabatic shear bands are universally observed in titanium alloy targets subjected to a projectile penetration; however, the underlying mechanism is not very clear. In this letter, the response of a Ti–6Al–4V plate against a 12.7-mm armor piercing projectile is investigated, both experimentally and computationally. By introducing a newly developed stress/strain coupling accumulation failure criterion, the cratering, ductile hole enlargement, and spalling processes are simulated, showing agreement with the experimental observations. The failures of the cratering and back spalling are due to the circumferential and tensile stress accumulation damage, whereas the ductile hole enlargement occurs as a result of the periodic loading–unloading cycle of the hydrostatic pressure, thus leading to a periodic array of shear bands. Further studies show that the von Mises stress is relatively stable during the penetration, and therefore the periodic change of hydrostatic pressure leads to the periodic stress triaxiality in the target, causing the periodic strain accumulation.

1. Introduction

Owing to their high specific strength and excellent combination of mechanical properties, corrosion resistance, and good ballistic performance, titanium alloys are a promising alternative for lightweight armor applications [1–3]. However, because of the low thermal conductivity, they are prone to form adiabatic shear bands (ASBs) under ballistic impact. The ASB is a narrow band that develops in the vast majority of ductile materials under a high strain rate loading. It results from the competition between strain hardening, strain rate hardening, and thermo softening. As the thermo-softening effect overcomes the strain and strain rate hardening effects, an uncontrolled failure occurs [4–6].

Understanding the formation process and the distribution of the ASBs is crucial in many applications. Numerous studies have been conducted, including both experimental and theoretical analyses, and the results are well documented. Nesterenko [7], and Zheng [8], as well as Martinez [9] and Lee [10], conducted several ballistic impact tests on the Ti–6Al–4V alloy under different conditions by using a variety of bullets and fragment-simulating projectiles. The results indicated that the ASBs manifest themselves in narrow, isolated, and periodical bands with a characteristic interspacing; they are also widely observed in high-speed machining [11] and radial collapse experiments of thick-walled cylinders [12]. Further observations of the optical metallograph views of the target cross sections reported by Sukumar [13] illustrated that the angle between the ASBs and the normal direction was approximately in the range of 43°–45°. The array of ASBs exhibited a self-organized pattern with a characteristic spacing between the bands, and the comparison of the average spacing indicated that the ASBs had a more intensive spatial distribution in the targets with higher hardness. Nesterenko et al. [12] investigated the ASBs by measuring the ASB spacing in different materials, and they found that the intervals of the ASBs in Ti–6Al–4V were wider than those observed in stainless steel because of its lower hardness. Besides, the evolution pattern of the ASBs was also different for greater variations of the mechanical properties. Analyzing the distribution features of the ASBs, Singh [14] and Sun [15] reported that the formation and distribution of the ASBs were related to the distribution of the maximum shear stress in the targets during the impact. Further work conducted by Murr [16] on ballistic tests indicated that the spacing of the ASBs in the target decreased with increasing the impact velocity.

The formation and distribution of the ASBs were also theoretically analyzed and a number of theory models were proposed. The models based on the perturbation theory and on the dynamic mechanical theory were proposed by Wright–Ockendon [17] and Grady–Kipp [18], respectively. Generally, the perturbation model is suitable to address the initiation stage of the shear bands, whereas the dynamic model provides higher precision on quantifying the spacing in the subsequent development of the ASBs. Subsequently, Molinari and Batra, as well as Daridon and Zhou [19], developed a series of mathematical schemes based on the aforementioned work; numerical approaches to analyze

* Corresponding author at: School of Materials Science and Engineering, Beijing Institute of Technology, Beijing 100081, China.
E-mail address: fanqunbo@bit.edu.cn (Q. Fan).

http://dx.doi.org/10.1016/j.matdes.2015.08.034

the formation of multiple ASBs in one dimension were also proposed [19,20].

Although progress has been made on understanding the formation and distribution of the ASBs, the underlying mechanism still requires further investigations. However, restricted by the current detecting methods, the experiments cannot directly capture the formation process of the ASBs during the impact process. On the other hand, the established theoretical models were based on some ideal assumptions, such as rate-independence linear thermal softening, or disregard of the strain hardening, and the results were inevitably limited in the description of the non-linear behavior of materials upon a high strain rate loading. Moreover, the theoretical models were unable to track the dynamic mechanical response and the damage evolution of the target. Fortunately, numerical simulations provide a powerful tool to analyze the microstructural evolution associated with the ASBs and adiabatic shear failure in ballistic tests. Although the formation process of the ASBs has been successfully modeled, most of the studies have focused on the formation of a single band under simple load conditions [21,22] or in a predetermined position, such as the dynamic compression of a hat-shaped specimen [23,24]. Until now, little research has been done on describing the evolution of multiple periodic ASBs under complex projectile-target interacting conditions. The manner in which the ASBs develop in the target under a ballistic impact is not very clear.

In the current study, by introducing a newly developed stress/strain coupling accumulation failure criterion, the failure process of the target and the phenomenon of the formation of periodical ASBs were successfully simulated. In contrast to the experimental and numerical results, the formation mechanism of the periodical ASBs was revealed from a mechanical point of view.

2. Experimental details

The selected material for the target plate is a Ti–6Al–4V alloy in solid solution and under aging treatment conditions. The titanium alloy is machined into a circular target plate with a normal thickness of 30 mm and a diameter of 80 mm. The projectile used in the present study is 12.7-mm armor piercing projectiles (AP) with ogival nose. It is made up of hardened tool steel T12 with hardness of about 56–62 HRC to keep its intact structure during the penetration process. The projectile was fired with a standard rifle from a distance of 10 m and the schematic of the experimental setup is shown in Fig. 1. The gun was mounted on a rigid mount with holding devices and properly aligned in a level plane to ensure the stability of ballistic tests and keep the angle of impact normal to the target plate. Six target plates were impacted under the same condition to guarantee the repeatability of the experiment. The velocities of impact were in the range of 800 ± 10 m/s, which were measured using infrared light emitting diode photovoltaic cells by testing the time interval between the interceptions caused by the projectile running across two transverse beams placed 2 m apart.

After the ballistic test, all impacted target plates were cut into halves through the mid-section of the crater and carefully observed. The results showed that they exhibited a similar failure pattern. Subsequently, the impacted plates were polished, and etched through standard metallographic techniques to observe the microstructure across the crater area.

3. Finite element analysis

3.1. Geometrical and material models

A numerical simulation of the Ti–6Al–4V plate impacted by the 12.7-mm AP was performed by using the explicit finite element code LS-DYNA, and the numerical configurations used in terms of dimensions and boundary conditions were based on the experimental setup. As shown in Fig. 2, the geometric model is finely and uniformly meshed with Shell 162 corresponding to a 4-node two-dimensional (2D) axisymmetric element; the reduced integration and a stiffness based hourglass control are also adopted. In the simulation, the projectile of hardened tool steel T12 is modeled as a rigid material for its non-deformation during the penetration. The material constants for the projectile are as follows: Density is 7850 kg/m^3; Young's modulus is 204 GPa; Poisson's ratio is 0.33. The dynamic behavior of the target is described by the Johnson–Cook constitutive model [25]. The material constants for Ti–6Al–4V used in the simulations are given in Table 1 [26]. Contact is established using the *CONTACT_2D_AUTOMATIC_SINGLE_SURFACE algorithm available in LS-DYNA. A small dynamic frictional coefficient of 0.05 is assumed between all surfaces in possible contact and no contact problems were found in the simulation using this algorithm. In the simulation, the projectile was given an initial velocity of 800 m/s which is similar to the one used in the corresponding experiments. To check the mesh sensitivity, simulations were carried out using four different element sizes of 1 mm, 0.5 mm, 0.33 mm and 0.25 mm, corresponding to 30, 60, 90 and 120 elements over the plate thickness. The results indicated that there were slightly mesh-size sensitive under such conditions, but the model converged monotonically toward a limit solution when the number of elements became sufficiently large. In order to reduce the computational time and ensure the calculation accuracy, the meshing size of the element in the target is selected to be 0.33 mm for subsequent analysis. Correspondingly, the total number of elements for the plate and projectile is 10,800 and 1005, respectively.

3.2. Failure criterion

Considering the comprehensive influence of the stress and strain on the cracking and failure of the material, a newly developed failure criterion that accounts for the accumulation damage of stress and strain is introduced to model the highly complex non-linear failure behavior of the target plate during the penetration. The fracture criterion

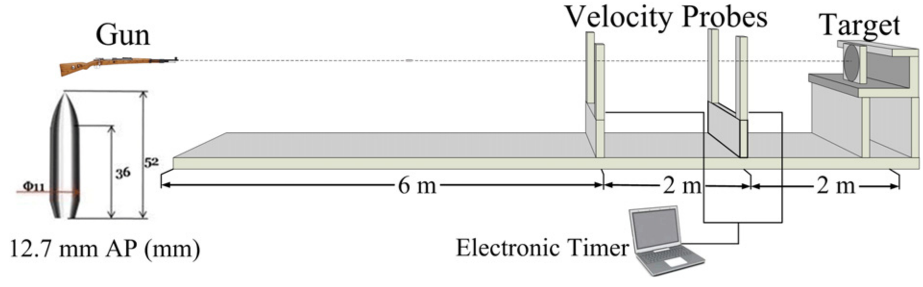

Fig. 1. Schematic of the experimental setup.

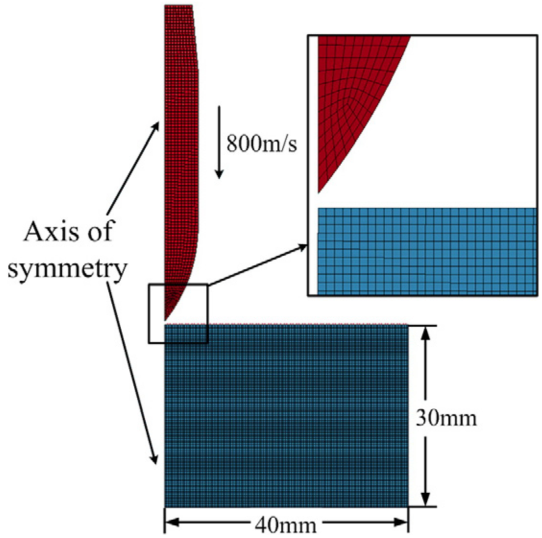

Fig. 2. The geometric model and definition of the meshes.

is expressed by Eq. (1), where D represents the accumulation of damage parameter and the fracture occurs when D reaches 1,

$$D = f(\sigma, \varepsilon) = \begin{cases} \int \frac{d\varepsilon_p}{\varepsilon_f(\sigma^*, \dot{\varepsilon}, T)} & (1-1) \\ \int \frac{[\max(0, \sigma_t - \sigma_0)]^A}{K} dt & (1-2) \end{cases} . \quad (1)$$

The evolution of the strain accumulation damage is implemented by the classic Johnson–Cook fracture criterion [27] that accounts for the conditions of stress triaxiality, strain rate, and temperature. As the accumulated plastic strain reaches the critical strain, failure occurs. The fracture strain is given by:

$$\varepsilon_f(\sigma^*, \dot{\varepsilon}, T) = [D_1 + D_2 \exp(D_3\sigma^*)]\left(1 + D_4 \ln\dot{\varepsilon}^*\right)(1 + D_5 T^*) \quad (2)$$

where D_1–D_5 are the failure parameters, $D_1 = -0.09$, $D_2 = 0.25$, $D_3 = -0.50$, $D_4 = 0.014$, $D_5 = 3.87$ [28]; $\sigma^* = p/\sigma_{eff}$ is the stress triaxiality, which can be expressed as the hydrostatic pressure divided by effective stress; $\dot{\varepsilon}^* = \dot{\varepsilon}/\dot{\varepsilon}_0$ is the non-dimensional plastic strain rate ($\dot{\varepsilon}_0 = 1.0\ \mathrm{s}^{-1}$); $T^* = (T - T_r)/(T_m - T_r)$ is the non-dimensional temperature (T_r and T_m are the room temperature and melt temperature, respectively).

The criterion of dynamical failure induced by the stress accumulation is described by Eqs. (1)–(2). This criterion assumes that the fracture phenomenon is not instantaneous, but requires a certain period of time. The material failure occurs when the maximum principal stress σ_t exceeds the threshold stress σ_0 and lasts for a certain period until the integral value reaches K. Stress values below the threshold value are too low to cause fracture even for very long duration. In our simulation, the parameters were obtained by static and dynamic tension experiments [29]. The material constants can be extracted via the curve fitting technique as $A = 2$, $\sigma_0 = 1000$ MPa, $K = 17\ \mathrm{MPa}^2 \cdot \mathrm{s}$.

Table 1
Johnson–Cook model parameters of Ti–6Al–4V.

ρ (kg/m^3)	E (GPa)	ν	C_p (J/kg·K)	T_m (K)	A (MPa)	B (MPa)	n	c	m
4428	110	0.41	580	1605	862	331	0.34	0.012	0.8

4. Results and discussion

4.1. Ballistic testing

Fig. 3 shows the typical macro morphology of the cross section along the penetration channel and the corresponding projectile after impact, indicating that the projectile entirely perforated the plate and the projectiles were hardly deformed in the ballistic tests. As we described in Section 2, the set up of ballistics tests were based on axial symmetry conditions. However, the nonsymmetry failure morphology of targets may be induced by the microstructure nonhomogeneity of the target material. The observation of the penetration channel reveals that the failure pattern of the target plate varies with the penetration depth, and three separate zones can be identified: (I) “Cratering Zone”, which is observed all along the periphery of the crater on the front face of the target. In this area, the crater presents a funnel shape and the angle of the crater surface to the horizontal plane is on average equal to 45°; (II) “Ductile Hole Enlargement Zone”, which is formed in the middle of the target plate. The penetration channel in this zone shows a smooth surface and the form of the channel is conical varying in diameter from 12 mm to 8.5 mm; (III) “Back Spalling Zone”, which is located on the rear surface of the target. The diameter of the spalling plate on the exit face is larger than the diameter of the projectile; delaminations are also observed in this zone.

4.2. Penetration process

A series of simulation results depicting the penetration process and the timeline are given in Fig. 4(a) and (b). Clearly, the aforementioned three stages are successfully simulated. Notably, each stage overlaps the next stage on the timeline, indicating that the different stages might occur simultaneously over a certain period of time. The cratering stage appears between 0 and 32 μs. At the beginning of this stage, the sharp nose of the projectile rapidly indents the front face of the target, and a plastic flow of the target material develops in the contact zone along the contour of the projectile nose because of the compression and shear loading, causing a slight uplift on the front face of the target near the impact area. Subsequently, the front face of the target cracks under the action of the projectile. At t = 18 μs, while the cratering stage is still evolving, the ductile hole enlargement stage begins and the ogival nose of the projectile fully penetrates the target. Between t = 18 and t = 35 μs, a severe plastic deformation and failure occur in the center of the target because of the extrusion of the hard nose, forming a penetration channel with the same diameter of the projectile. The back spalling is the last stage of the penetration process; it begins at t = 28 μs and terminates at t = 42 μs when the spalling body flies out of the target. The initiation of the back spalling is caused by the dynamic tensile stress in the rare surface of the target. During the very beginning instant of impact, a shock wave is induced in the normal direction and radially out of the impact spot. The shock wave front propagates toward the rare surface and reflects, and the velocity D can be estimated by using the linear relationship $D = c_0 + s \cdot u$ [30], where c_0 is the speed of elastic wave, u is particle velocity and s is the parameter of Mie Grüneisen equation of state. Thus, $D = 5000\ \mathrm{m/s} + 0.767 \times 600\ \mathrm{m/s} \approx 5500\ \mathrm{m/s}$. Since the thickness of the plate is 30 mm, the first shock wave should reflect at the rare surface at about 5–6 μs. According to the numerical simulation results, however, the back spalling happens until t = 28 μs, indicating that only at 28 μs the stress exceeds the ability of the material to maintain its integrity due to enough stress accumulation. In the final stage, the cracks initiate on the back surface approximately 7 mm away from the axis of the target and propagate toward the inner plate until they aggregate and form a cone-shaped spalling body. As the projectile penetrates through the backside of the target plate, the spalling body is pushed out and a back spalling zone forms. Interestingly, the cratering stage, the ductile hole enlargement stage, and the

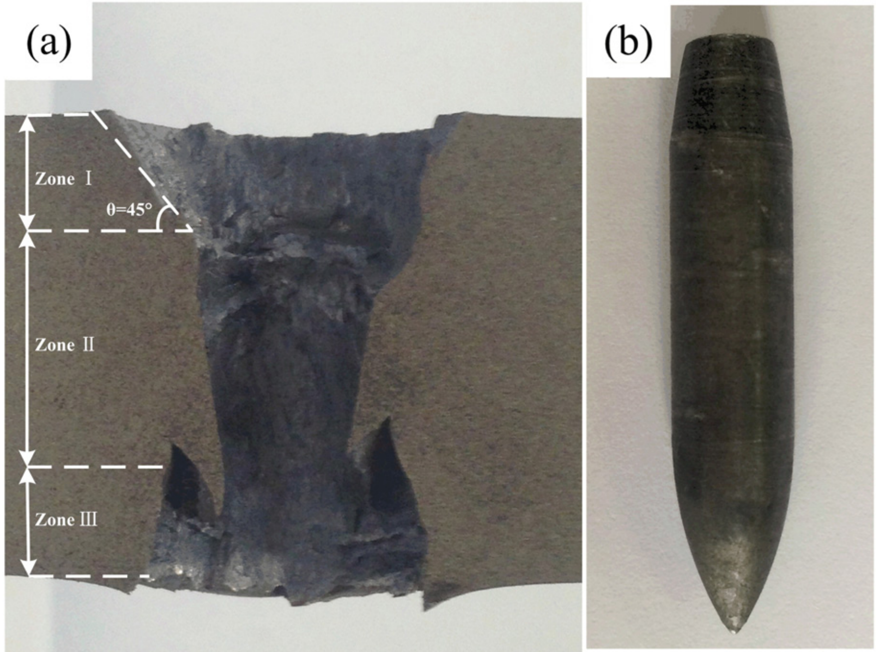

Fig. 3. Macro morphologies of the cross section along the penetration channel and the corresponding projectile after impact. (a) The sectioned view of the penetration channel labeled with three separate zones;(b) the projectile after impact.

back spalling stage occur simultaneously between 28 μs and 32 μs. At that time, the accumulation of tensile stress in the free surface of the target and the plastic deformation of the material in the middle of the target meet the failure criterion respectively. Such experimental phenomenon was also observed in the ballistic tests conducted by Dikshit [31] and Børvik [32].

The physical behaviors of the target plate during the penetration and perforation is basically coincided with the simulation results even though the numerical results don't correspond to the experimental results in details. Yet the computational model can still be used to conduct an evaluation and mechanism analysis of the penetration process.

4.3. Failure mechanism

Fig. 5 shows the contour of the first principal stress in the target plate at $t = 29$ μs, an exemplary time during the penetration process. Clearly, different stress states are found in different regions of the target. The material near the free surfaces of the target, such as in Cratering Zone I and Back Spalling Zone III, is in a state of tension and the peak values are about 1400–1600 MPa. Conversely, in Ductile Hole Enlargement Zone II, the material is under a compressive stress, and the maximum stress in this region reaches 1800 MPa.

In order to see the stress distributions more clearly from the three-dimensional perspective view, some elements of the three typical

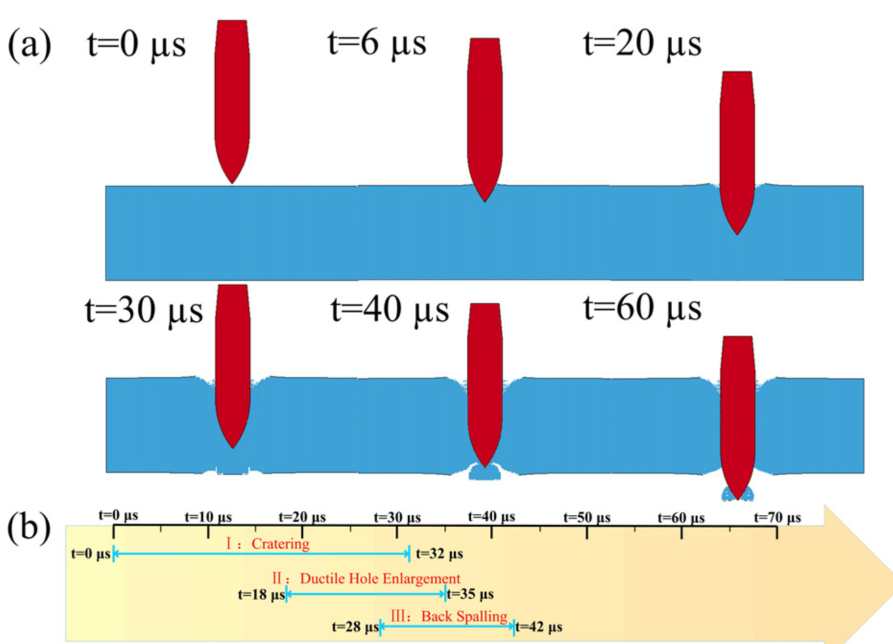

Fig. 4. The simulation results depicting the penetration process. (a) The representative images of the simulation results; (b) the timeline of the penetration process.

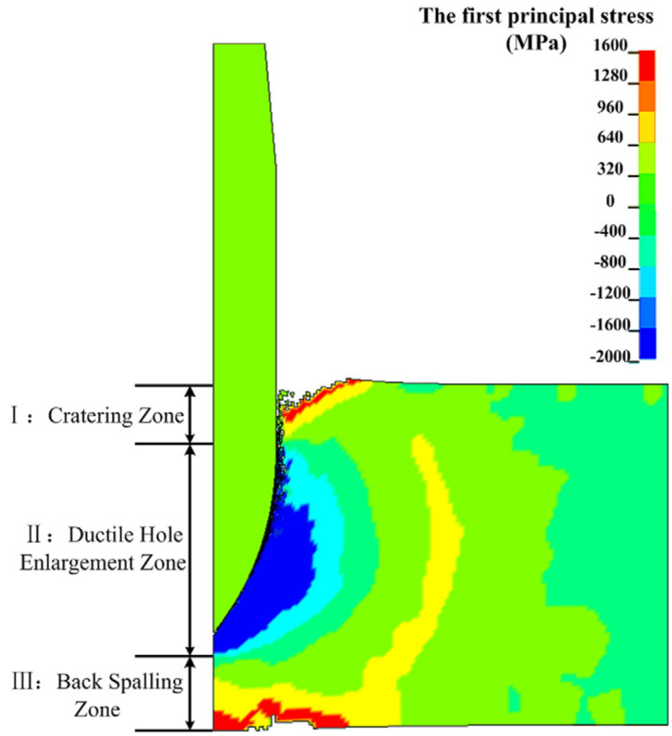

Fig. 5. The contour of the first principal stress in the target plate at t = 29 μs.

regions in the two-dimensional section are selected, magnified, rotated and indicated by using vectors of the first principle stresses at t = 29 μs, where the stress directions and magnitudes are signed by a serial of arrows, as shown in Fig. 6. Notably, Zone I and Zone III are subjected to a circumferential tensile stress in a direction of normal to the section plane of the target, and the material in these regions undergoes a small deformation without directly interacting with the projectile. Such behavior reveals that the material in these regions fails because of the stress accumulation. However, the material in Zone II suffers from a circumferential and radial compressive stress and severe deformations, indicating that the material in this location bears a high plastic deformation under a state of compression. Thus, the plastic strain accumulates in those severely deformed elements, eventually reaching the failure criteria. The accumulated plastic strain in this region could lead to an adiabatic temperature rise, and, as the thermo-softening effect overcomes the rate of the strain hardening effect, the ASBs are formed.

Fig. 7 shows the optical microstructures of the cross section of the target plate. The ASBs are not found in Cratering Zone I and Back Spalling Zone III, but a number of ASBs are clearly observed in Ductile Hole Enlargement Zone II. The ASBs distribute regularly with an averaged spacing of 2.5–3 mm in the range of 8–25 mm along the penetration channel; the angle between each ASB and the penetration direction is approximately 45°.

To reveal the underlying mechanism of the periodic ASB phenomenon along the axis of the target plate, the histories of the plastic strain, the von Mises effective stress and the hydrostatic pressure of the target elements along the central axis can be tracked. In the penetration process, strong interaction between the target and the projectile, especially along the central axis, will take place. So the corresponding penetration depth, namely the moving position of the projectile nose tip, can be regarded as the exact locations of target nodes along the central axis when the projectile just arrives at it. Fig. 8 shows the evolution for the three parameters at corresponding penetration depth. The abscissa of the coordinate system is the penetration depth, and the ordinate

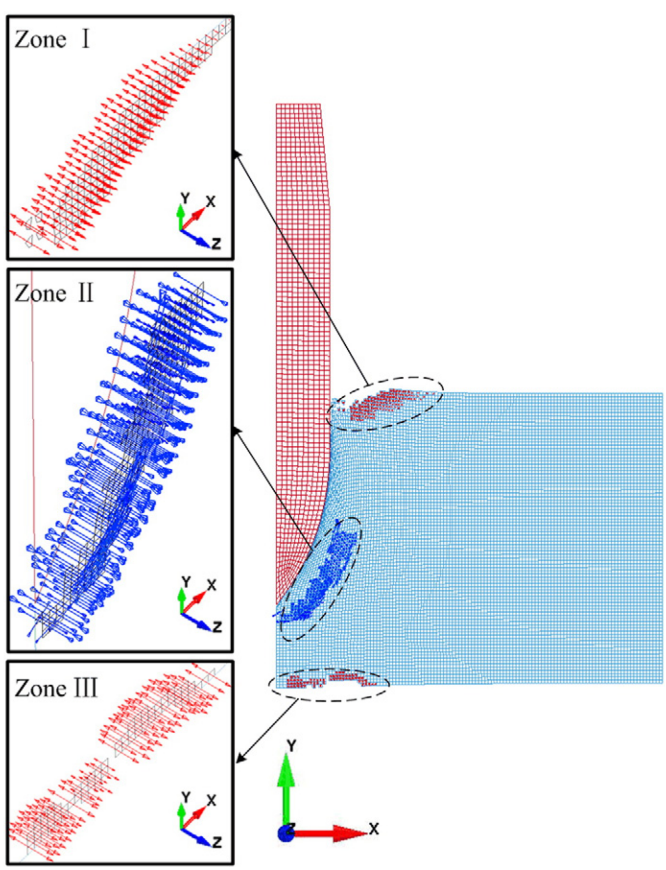

Fig. 6. Vectors of the first principle stresses in three typical zones of the target at t = 29 μs.

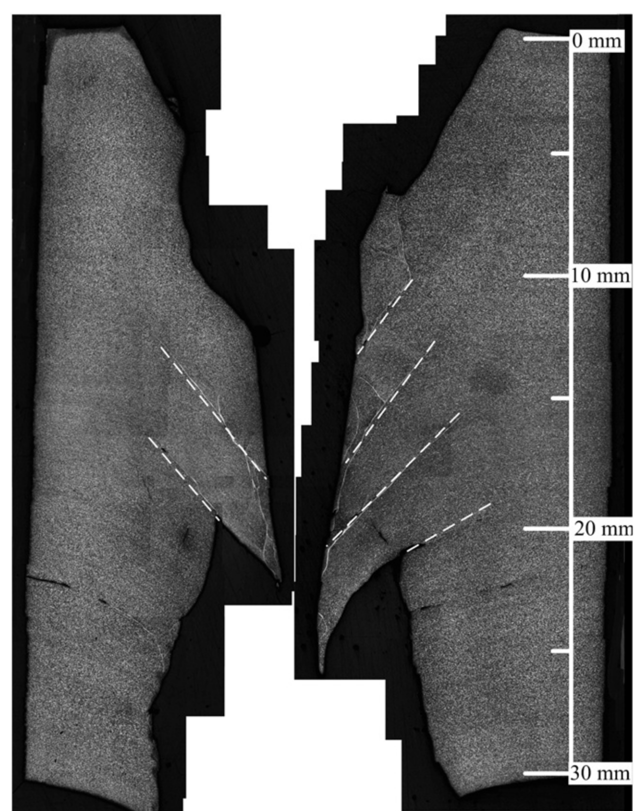

Fig. 7. The microstructures of the cross-section of the target plate.

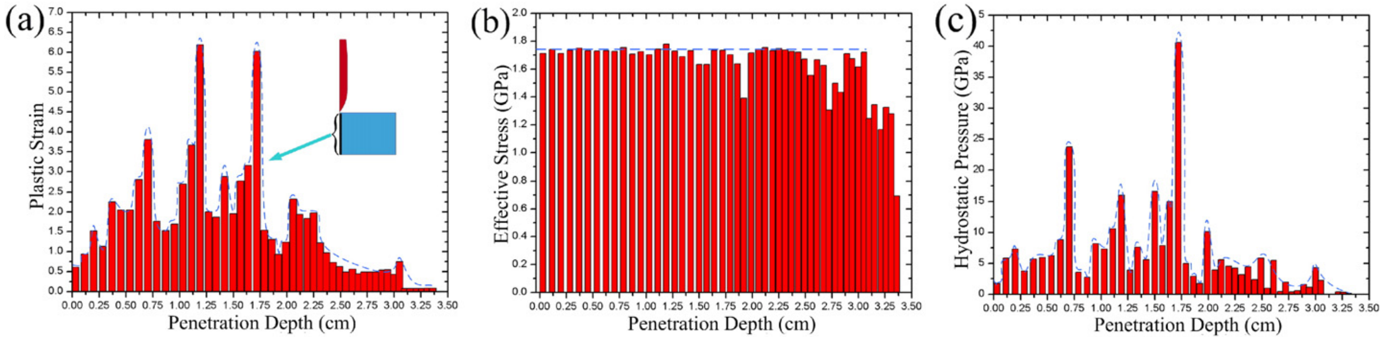

Fig. 8. Evolution for the three parameters of the target elements along the central axis at corresponding penetration depth: (a) the plastic strain; (b) the effective stress; (c) the hydrostatic pressure.

shows corresponding values extracted from elements before they are fractured and deleted in the model. In Fig. 8(a) and its inset a total of 50 plastic strain values are illustrated. The blue line indicating the envelope of all the strain value shows that the strain peaks appear periodically during the penetration, and the first peak is 7.3 mm away from the front surface. The maximum value of the strain peak is above 6, indicating that severe plastic deformation occurs at the corresponding element. Moreover, the strain peaks have a spacing of 2.5–5 mm and distribute primarily in the range of 10–20 mm along the penetration channel; both values are in reasonable agreement with the observed ASB distribution in Fig. 7. Clearly, the simulated periodic strain peaks can be used to accurately predict the formation of the ASBs.

As shown in Fig. 8(b), the effective stresses of the elements along the target axis are basically identical and approximately equal to 1.7 GPa when the projectile arrives at the corresponding element. As shown in Fig. 8(c), however, the hydrostatic pressure presents a distribution similar to that of the plastic strain, and the peak positions of the pressure are found consistent with the locations of the plastic strain peaks. As stated in Eq. (2), the stress triaxiality is the ratio of the hydrostatic pressure divided by the effective stress, which is an important factor that influences the accumulated strain failure criterion. If the elements experience an identical effective stress, their strain failure criterion will be determined by the hydrostatic pressure. The higher the hydrostatic pressure, the higher the strain failure criterion, and severe plastic deformations or ASBs will be induced along the penetration channel. Once the severely deformed element reaches the threshold strain, it will be removed from the model, and the extremely high hydrostatic pressure is unloaded. Subsequently, the hydrostatic pressure accumulates once again during the next interaction of the projectile nose with the target material until the next strain peak reaches the failure criterion. Therefore, such a periodic loading–unloading cycle of the hydrostatic pressure in the target constitutes the mechanical mechanism behind the development of multiple periodical ASBs.

5. Conclusions

In this study, we have analyzed, both experimentally and numerically, the response of a Ti–6Al–4V plate against a 12.7-mm AP. The ballistic impact process exhibited three typical stages: cratering stage, ductile hole enlargement stage, and back spalling stage; different stages might occur simultaneously over a certain period of time. The tensile and radial stress accumulation induces the formation of Cratering Zone and Back Spalling Zone, whereas the strain accumulative failure is the underlying mechanism for the formation of Ductile Hole Enlargement Zone. Further numerical results reveal that the periodic loading–unloading cycle of the hydrostatic pressure leads to the formation of multiple periodical ASBs, which is related to the triaxiality and the periodic strain failure criterion.

Acknowledgment

We gratefully acknowledge the financial support of the program for New Century Excellent Talents in University (NCET-12-0051).

References

[1] J.S. Montgomery, M.G.H. Wells, Titanium armor applications in combat vehicles, JOM 53 (4) (2001) 29–32.
[2] R. Li, Q. Fan, R. Gao, L. Huo, F. Wang, Y. Wang, Effects of dynamic mechanical properties on the ballistic performance of a new near-β titanium alloy Ti684, Mater. Des. 62 (2014) 233–240.
[3] K. Sun, X. Yu, C. Tan, H. Ma, F. Wang, H. Cai, Influence of adiabatic shear bands intersection on the ballistic impact of Ti–6Al–4V alloys with three microstructures, Mater. Sci. Eng. A 606 (2014) 257–267.
[4] Y.L. Bai, B. Dodd, Adiabatic Shear Localization, Pergamon Press, Oxford, 1992.
[5] A.R. Shahan, A.K. Taheri, Adiabatic shear bands in titanium and titanium alloys: a critical review, Mater. Des. 14 (4) (1993) 243–250.
[6] E. Roux, P. Longère, O. Cherrier, T. Millot, D. Capdeville, J. Petit, Analysis of ASB assisted failure in a high strength steel under high loading rate, Mater. Des. 75 (2015) 149–159.
[7] V.F. Nesterenko, W. Goldsmith, S.S. Indrakanti, Y.B. Gu, Response of hot isostatically pressed Ti–6Al–4V targets to normal impact by conical and blunt projectiles, Int. J. Impact Eng. 28 (2003) 137–160.
[8] C. Zheng, F. Wang, X. Cheng, K. Fu, J. Liu, Y. Wang, Effect of microstructures on ballistic impact property of Ti–6Al–4V targets, Mater. Sci. Eng. A 608 (2014) 53–62.
[9] F. Martinez, L.E. Murr, A. Ramirez, M.I. Lopez, S.M. Gaytan, Dynamic deformation and adiabatic shear microstructures associated with ballistic plug formation and fracture in Ti–6Al–4V targets, Mater. Sci. Eng. A 454–455 (2007) 581–589.
[10] D.G. Lee, Y.H. Lee, S. Lee, C.S. Lee, S.M. Hur, Dynamic deformation behavior and ballistic impact properties of Ti–6Al–4V alloy having equiaxed and bimodal microstructures, Metall. Mater. Trans. A 35A (2004) 3103–3112.
[11] G.G. Ye, S.F. Xue, M.Q. Jiang, X.H. Tong, L.H. Dai, Modeling periodic adiabatic shear band evolution during high speed machining Ti–6Al–4V alloy, Int. J. Plast. 40 (2013) 39–55.
[12] Q. Xue, M.A. Meyers, V.F. Nesterenko, Self-organization of shear bands in titanium and Ti–6Al–4V alloy, Acta Mater. 50 (3) (2002) 575–596.
[13] G. Sukumar, B.B. Singh, A. Bhattacharjee, K.S. Kumar, A.K. Gogia, Ballistic impact behavior of β-CEZ Ti alloy against 7.62 mm armour piercing projectiles, Int. J. Impact Eng. 54 (2013) 149–160.
[14] B.B. Singh, G. Sukumar, A. Bhattacharjee, K.S. Kumar, T.B. Bhat, A.K. Gogia, Effect of heat treatment on ballistic impact behavior of Ti–6Al–4V against 7.62 mm deformable projectile, Mater. Des. 36 (2012) 640–649.
[15] K. Sun, X. Yu, C. Tan, H. Ma, F. Wang, H. Cai, Effect of microstructure on adiabatic shear band bifurcation in Ti–6Al–4V alloys under ballistic impact, Mater. Sci. Eng. A 595 (2014) 247–256.
[16] L.E. Murr, A.C. Ramirez, S.M. Gaytan, M.I. Lopez, E.Y. Martinez, D.H. Hernandez, et al., Microstructure evolution associated with adiabatic shear bands and shear band failure in ballistic plug formation in Ti–6Al–4V targets, Mater. Sci. Eng. A 516 (1–2) (2009) 205–216.
[17] T.W. Wright, H. Ockendon, A scaling law for the effect of inertia on the formation of adiabatic shear bands, Int. J. Plast. 12 (7) (1996) 927–934.
[18] D.E. Grady, M.E. Kipp, The growth of unstable thermoplastic shear with application to steady-wave shock compression in solids, J. Mech. Phys. Solids 35 (1) (1987) 95–119.
[19] F. Zhou, T.W. Wright, K.T. Ramesh, The formation of multiple adiabatic shear bands, J. Mech. Phys. Solids 54 (7) (2006) 1376–1400.
[20] J.W. Walter, Numerical experiments on adiabatic shear band formation in one dimension, Int. J. Plast. 8 (6) (1992) 657–693.
[21] M. Fermen-Coker, Numerical simulation of adiabatic shear bands in Ti–6Al–4V alloy due to fragment impact, Army Research Laboratory2004 1–3.

[22] M. Dolinski, D. Rittel, Experiments and modeling of ballistic penetration using an energy failure criterion, J. Mech. Phys. Solids 83 (2015) 1–18.
[23] A. Khosravifard, M.M. Moshksar, R. Ebrahimi, High strain rate torsional testing of a high manganese steel: design and simulation, Mater. Des. 52 (2013) 495–503.
[24] Y. Xu, J. Chen, Atomistic potentials based energy flux integral criterion for dynamic adiabatic shear banding, J. Mech. Phys. Solids 75 (2015) 45–57.
[25] G.R. Johnson, W.H. Cook, A constitutive model and data for metals subjected to large strains, high strain rates and high temperatures, Proceedings of the 7th International Symposium on Ballistics, American Defense Preparedness Association, Hague, Netherlands, 1983 541–547.
[26] D.R. Lesuer, Experimental Investigations of Material Models for Ti–6Al–4V Titanium and 2024-T3 Aluminum, Lawrence Livermore National Laboratory, 2000 1–41.
[27] G.R. Johnson, W.H. Cook, Fracture characteristics of three metals subjected to various strains, strain rates, temperatures and pressures, Eng. Fract. Mech. 21 (1) (1985) 31–48.
[28] G.R. Johnson, T.J. Holmquist, Test Data and Computational Strength and Fracture Model Constants for 23 Materials Subjected to Large Strains, High Strain Rates and High Temperatures, Los Alamos National Laboratory Report, 1989 (LA-11463-MS.).
[29] J. Jeong, H. Adib, G. Pluvinage, Proposal of new damage model for thermal shock based on dynamic fracture on the brittle materials, J. Non-Cryst. Solids 351 (24–26) (2005) 2065–2075.
[30] Y.B. Zel'dovich, Y.P. Raizer, Physics of Shock Waves and High-Temperature Hydrodynamic Phenomena Vol I, Academic, New York, 1966.
[31] S.N. Dikshit, V.V. Kutumbarao, G. Sundararajan, The influence of plate hardness on the ballistic penetration of thick steel plates, Int. J. Impact Eng. 16 (2) (1995) 293–320.
[32] T. Børvik, A.H. Clausen, O.S. Hopperstad, M. Langseth, Perforation of AA5083-H116 aluminium plates with conical-nose steel projectiles—experimental study, Int. J. Impact Eng. 30 (2004) 367–384.